Scheme for contact angle and its hysteresis in a multiphase lattice Boltzmann method

Lei Wang, Hai-bo Huang,* and Xi-Yun Lu

Department of Modern Mechanics, University of Science and Technology of China, Hefei, Anhui 230026, China

(Received 3 July 2012; revised manuscript received 20 October 2012; published 3 January 2013)

In this paper, a scheme for specifying contact angle and its hysteresis is incorporated into a multiphase lattice Boltzmann method. The scheme is validated through investigations of the dynamic behaviors of a droplet sliding along two kinds of walls: a smooth (ideal) wall and a rough or chemically inhomogeneous (nonideal) wall. For an ideal wall, the wettability of solid substrates is able to be prescribed. For a nonideal wall, arbitrary contact angle hysteresis can be obtained through adjusting advancing and receding angles. Significantly different phenomena can be recovered for the two kinds of walls. For instance, a droplet on an inclined ideal wall under gravity is impossible to stay stationary. However, the droplet on a nonideal wall may be pinned due to contact angle hysteresis. The steady interface shapes of the droplet on an inclined nonideal wall under gravity or in a shear flow quantitatively agree well with the previous numerical studies. Besides, the complex motion of a droplet creeping like an inchworm could be simulated. The scheme is found suitable for the study of contact line problems with and without contact angle hysteresis.

DOI: 10.1103/PhysRevE.87.013301 PACS number(s): 47.11.−j, 47.55.np, 47.61.Jd

I. INTRODUCTION

Droplets sliding on a solid wall is a common phenomenon in nature and in engineering applications, such as drops of dew rolling on leaves, crude oil attached to rocks, pesticide spreading over plants, and so on. These fundamental problems have been studied with different numerical methods [1–6]. For instance, Dimitrakopoulos and Higdon studied displacement of 2D or 3D fluid droplets on solid surfaces in different flows [7–10] using the spectral boundary element method; Ding *et al.* used diffuse interface method to study the dynamical behaviors of a 3D droplet on a wall in shear flows [11]; Spelt used a level-set approach for simulations of flows with multiple moving contact lines with hysteresis [12]; Schleizer *et al.* used boundary-integral method to investigate 2D droplet subject to shear and pressure-driven flows [13]. Recently, lattice Boltzmann method (LBM) has also been applied in these research areas [14–19]. Compared to the above traditional numerical methods based on discretizations of macroscopic continuum equations, the LBM does not require solving the Poisson equation. It is an explicit scheme and easy to parallelize.

Since the 1980s, several multiphase LBMs have emerged [20–27], such as the Shan-and-Chen-type model [22,23], the color-gradient model [20,21], the free-energy model [24,26], and the model proposed by He, Chen, and Zhang (He-Chen-Zhang model) [25,27]. The color-gradient model was proposed by Rothman and Keller [20], in which a recolor step is implemented to separate fluids (distinguished by red and blue) with different colors and the ratio of densities is limited to unity. The Shan-and-Chen-type LB model, which introduced potentials between particles to model fluid flows, may be the simplest one [22,23]. The He-Chen-Zhang model is based on the idea of the level-set method [25]. Later, Lee and Lin further developed the above model and achieved high density ratio through a stable discretization of the lattice Boltzmann equation (Lee-Lin model) [27].

Due to mesoscopic property, the above multiphase LBMs have some advantages over conventional methods for multiphase flows [28–32]. Hence, they are also used to model contact line dynamics [29–32]. With the Shan-Chen model, Kang *et al.* studied 2D droplets sliding on smooth walls and investigated effects of the wettability, Bond number, droplet size, and density and viscosity ratios of two phases [14]. Zhang *et al.* [16] and Fan *et al.* [33] studied the function between the apparent contact angle and the velocity of displacement in a channel with a mean-field free-energy model and the Shan-Chen model, respectively.

For nonideal wall, Iwahara *et al.* used the two-dimensional model of Inamuro *et al.* [26] to study droplets on homogeneous and chemically heterogeneous surfaces [15]. Kim *et al.* also used the model of Inamuro *et al.* [26] to investigate water droplet properties on rough surfaces with periodical distributions of pillars [19]. Kusumaatmaja and Yeomans studied the droplet deformation when it passes through an array of hydrophilic strips of different widths [29]. They also studied the dynamics of liquid drops on a superhydrophobic surface patterned with sawtooth ridges or posts [32]. Pirat *et al.* studied the droplet movement in a patterned surface using the Shan-Chen model [31]. Varnik *et al.* investigated the droplet movement when it passes through strips with different wetting properties [30]. However, most of the above studies intend to investigate hysteresis microscopically. Besides, in the study of Pirat *et al.* [31], high resolution for complex solid boundaries may require huge computational cost. Hence, their applications are highly limited.

Recently, Colosqui *et al.* [28] also investigated the contact angle hysteresis using a LBM. Their simulation presents a thin surface film, within which a disjoining pressure acts. By modifying the form of the disjoining pressure, one can vary the static and dynamic hysteresis on surfaces that exhibit the same equilibrium contact angle [28]. However, in their study, the description is mesoscopic. How to connect the hysteresis parameters in the model with the macroscopic hysteresis window (advancing and receding angles) is unknown.

Here, we focus on the macroscopic characteristic of hysteresis, which is described by advancing and receding

*huanghb@ustc.edu.cn

angles directly no matter what causes the hysteresis. The advancing and receding angles could be specified in our scheme arbitrarily. For wettability of solids, usually the surface-energy approach is used to obtain contact angle, which is determined by Young's equation [5,34,35]. However, it has been shown that a slope of the interface resulted from the surface-energy approach is not in accord with the prescribed contact angle [36]. Recently, Ding *et al.* proposed a formulation that is derived from the geometry of interphase around the triple line and the geometrical formulation indeed resulted in the prescribed contact angle [36].

In this paper, we incorporate the scheme proposed by Ding *et al.* into the He-Chen-Zhang model [25] and Lee-Lin model [27]. In our scheme, the desired contact angle can be easily obtained for ideal surfaces and contact angle hysteresis effect can be realized for nonideal surfaces. The numerical method will be described in detail in Sec. II.

II. MATHEMATICAL FORMULATION AND NUMERICAL METHODS

A. Lattice Boltzmann method for two-phase flows

The multiphase LBM used here was proposed by He *et al.*, in which an index function is used to track interfaces between liquid and gas [25]. In the model, molecular interaction is incorporated to simulate interfacial dynamics. Two distribution functions, $\bar{f}_i$ and $\bar{g}_i$, are introduced, which are able to recover the Cahn-Hilliard equation (evolution of the index function) and Navier-Stokes equations, respectively.

$$\begin{aligned}\bar{f}_i(\boldsymbol{x}+\boldsymbol{e}_i\delta t,t+\delta t)-\bar{f}_i(\boldsymbol{x},t)&=-\frac{\bar{f}_i(\boldsymbol{x},t)-f_i^{\mathrm{eq}}(\boldsymbol{x},t)}{\tau}\\&\quad-\frac{(2\tau-1)}{2\tau}\frac{(\boldsymbol{e}_i-\boldsymbol{u})\cdot\nabla\psi(\phi)}{RT}\Gamma_i(\boldsymbol{u})\delta t,\end{aligned}\tag{1}$$

$$\begin{aligned}&\bar{g}_i(\boldsymbol{x}+\boldsymbol{e}_i\delta t,t+\delta t)-\bar{g}_i(\boldsymbol{x},t)\\&=-\frac{\bar{g}_i(\boldsymbol{x},t)-g_i^{\mathrm{eq}}(\boldsymbol{x},t)}{\tau}+\frac{(2\tau-1)}{2\tau}(\boldsymbol{e}_i-\boldsymbol{u})\{\Gamma_i(\boldsymbol{u})(\boldsymbol{F}_s+\boldsymbol{G})\\&\quad-[\Gamma_i(\boldsymbol{u})-\Gamma_i(0)]\nabla\psi(\rho)\}\delta t,\end{aligned}\tag{2}$$

where $\boldsymbol{e}_i$ is discrete velocity, for the D2Q9 velocity model,

$$[\mathbf{e}_0,\mathbf{e}_1,\mathbf{e}_2,\mathbf{e}_3,\mathbf{e}_4,\mathbf{e}_5,\mathbf{e}_6,\mathbf{e}_7,\mathbf{e}_8]=\begin{bmatrix}0&1&0&-1&0&1&-1&-1&1\\0&0&1&0&-1&1&1&-1&-1\end{bmatrix}.$$

For the 3D simulations, the D3Q15 velocity model [37] is used because it requires less memory. In the above equations, $c=\delta x/\delta t$ is the lattice speed, where δx is the lattice unit (l.u.) and δt is the time step (t.s.). $c_s=c/\sqrt{3}$ is the sound speed. τ is a nondimensional relaxation time, which is related to the kinematic viscosity by $\nu=c_s^2(\tau-0.5)\delta t$. $\boldsymbol{F}_s=\kappa\rho\nabla\nabla^2\rho$ denotes surface tension, where ρ is the density of the fluid and κ controls the strength of surface tension. $\boldsymbol{G}$ is the body force.

The equilibrium distribution functions f_i^{eq} and g_i^{eq} can be computed as,

$$f_i^{\mathrm{eq}}=\omega_i\phi\left[1+\frac{3\boldsymbol{e}_i\cdot\boldsymbol{u}}{c^2}+\frac{9(\boldsymbol{e}_i\cdot\boldsymbol{u})^2}{2c^4}-\frac{3\boldsymbol{u}^2}{2c^2}\right],\tag{3}$$

$$g_i^{\mathrm{eq}}=\omega_i\left[p+\rho c_s^2\left(\frac{3\boldsymbol{e}_i\cdot\boldsymbol{u}}{c^2}+\frac{9(\boldsymbol{e}_i\cdot\boldsymbol{u})^2}{2c^4}-\frac{3\boldsymbol{u}^2}{2c^2}\right)\right],\tag{4}$$

where ϕ and p are index function and pressure, respectively. The weighting factors are given by $\omega_i=4/9\,(i=0)$, $\omega_i=1/9\,(i=1,2,3,4)$, and $\omega_i=1/36\,(i=5,6,7,8)$.

In Eq. (2), $\Gamma_i(\boldsymbol{u})$ and $\psi(\rho)$ are defined as

$$\Gamma_i(\boldsymbol{u})=\omega_i\left[1+\frac{3\boldsymbol{e}_i\cdot\boldsymbol{u}}{c^2}+\frac{9(\boldsymbol{e}_i\cdot\boldsymbol{u})^2}{2c^4}-\frac{3\boldsymbol{u}^2}{2c^2}\right],\tag{5}$$

$$\psi(\rho)=p-\rho RT.\tag{6}$$

In this model, the Carnahan-Starling equation of state is incorporated, i.e.,

$$p=\rho RT\frac{1+b\rho/4+(b\rho/4)^2-(b\rho/4)^3}{(1-b\rho/4)^3}-a\rho^2,\tag{7}$$

where $RT=c_s^2$. In our simulations, a and b are set to be $12RT$ and 4, respectively.

The macroscopic variables can be obtained by

$$\phi=\sum\bar{f}_i,\tag{8}$$

$$p=\sum\bar{g}_i-\frac{1}{2}\boldsymbol{u}\cdot\nabla\psi(\rho)\delta t,\tag{9}$$

$$\rho RT\boldsymbol{u}=\sum\boldsymbol{e}_i\bar{g}_i+\frac{RT}{2}(\boldsymbol{F}_s+\boldsymbol{G})\delta t.\tag{10}$$

Once the index function $\phi(\mathbf{x},t)$ is known, we can easily obtain the density (ρ), kinematic viscosity(ν) of fluids, and relaxation factor τ, according to the following formulations:

$$\rho(\phi)=\rho_g+\frac{\phi-\phi_{\min}}{\phi_{\max}-\phi_{\min}}(\rho_l-\rho_g),\tag{11}$$

$$\nu(\phi)=\nu_g+\frac{\phi-\phi_{\min}}{\phi_{\max}-\phi_{\min}}(\nu_l-\nu_g),\tag{12}$$

$$\tau(\phi)=\tau_g+\frac{\phi-\phi_{\min}}{\phi_{\max}-\phi_{\min}}(\tau_l-\tau_g),\tag{13}$$

where ρ_l and ρ_g denote the densities of liquid and gas, respectively; ν_l and ν_g denote the kinematic viscosities of liquid and gas, respectively; τ_l and τ_g denote the nondimensional relaxation times of liquid and gas, respectively. $\phi_{\max}$ and $\phi_{\min}$ are the maximal and the minimum values of the index function. In the He-Chen-Zhang model, we choose $\phi_{\max}=0.251$, $\phi_{\min}=0.024$, $\rho_l=0.251$, $\rho_g=0.024$ in the simulations [38], so the density ratio is about 10.46.

The model developed by Lee and Lin [27] is also used to simulate multiphase flows. The model is almost identical as the He-Chen-Zhang model except the directional derivatives are introduced and the collision step is split into two substeps: prestream and poststream collisions.

B. Contact angle and its hysteresis

For an equilibrium contact angle on an ideal solid wall, the interfacial tensions are in balance at the contact point of three phases. The interfacial tensions and the contact angle satisfy Young's equation. In traditional numerical methods, the surface-energy formulation is usually used for implementation of wetting condition [34,35,39]. However, the scheme of using geometric formulation has advantages over the surface-energy

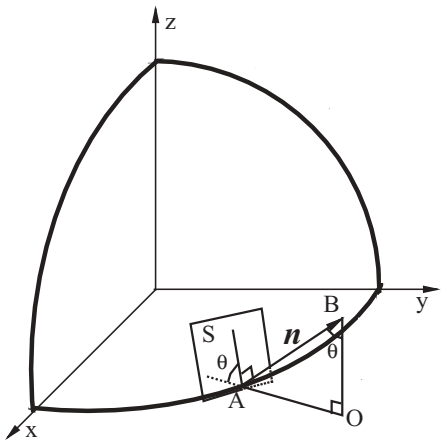

FIG. 1. Schematic of contact angle in 3D situations.

formulation [36]. Therefore, the geometric formulation is adopted in this paper. The formulation is [36]

$$\phi_{i,1} = \phi_{i,3} + \tan\left(\frac{\pi}{2} - \theta\right)|\phi_{i+1,2} - \phi_{i-1,2}|, \qquad (14)$$

where the first and second subscripts denote the coordinates along and normal to the solid boundary, respectively. θ is the desired contact angle. In order to calculate the terms of $\nabla\psi(\phi)$ and $\nabla\psi(\rho)$, a layer of ghost cells adjacent to the solid boundary is necessary. The values of $\phi_{i,0}$, defined on the ghost cells, are given by $\phi_{i,0} = \phi_{i,1}$.

For 3D simulations, the extension of Eq. (14) is straightforward. Schematic of the 3D situation is shown in Fig. 1, in which the x-y plane is supposed to be a wall and "A" is a point in the contact line. The gradient of ϕ at point A is $-\boldsymbol{n} = (\frac{\partial\phi}{\partial x}, \frac{\partial\phi}{\partial y}, \frac{\partial\phi}{\partial z})$ for the cases of a droplet inside gas. A tangent plane "S" on the droplet surface, which passes through point A, is also illustrated. The plane is supposed to be perpendicular to the vector $\boldsymbol{n}$. As illustrated in Fig. 1, the contact angle between the wall and the interface, i.e., θ satisfies $\tan(\frac{\pi}{2} - \theta) = \frac{\overline{OB}}{\overline{OA}} = -\frac{\partial\phi}{\partial z}/\sqrt{(\frac{\partial\phi}{\partial x})^2 + (\frac{\partial\phi}{\partial y})^2}$, where the overline means the length of the line. This equation would lead to the following discrete form,

$$\phi_{i,j,1} = \phi_{i,j,3} + \tan\left(\frac{\pi}{2} - \theta\right)\xi, \qquad (15)$$

where

$$\xi = \sqrt{(\phi_{i+1,j,2} - \phi_{i-1,j,2})^2 + (\phi_{i,j+1,2} - \phi_{i,j-1,2})^2}. \qquad (16)$$

In the above way, we can achieve any wettability between fluids and solids through inputting a specified contact angle ($0^\circ \leqslant \theta \leqslant 180^\circ$) into Eq. (14) and Eq. (15) for 2D and 3D cases, respectively. It is noted that Eqs. (14) and (15) are applied only at the contact point and the contact line, respectively.

On the other hand, in many natural and industry systems, the solid walls are usually rough and chemically inhomogeneous [40]. So, we further extend the above geometric formulation to the no-ideal surfaces. In other words, contact angle hysteresis is taken into consideration. Due to hysteresis, the contact line remains pinned when the local contact angle θ is within a hysteresis window [6,9],

$$\theta_R \leqslant \theta \leqslant \theta_A, \qquad (17)$$

where θ_R and θ_A denote the receding angle and advancing angle, respectively. But if θ is not inside the hysteresis window, the contact line is allowed to move [41]. When θ is greater than θ_A, the contact line moves forward; when θ is less than θ_R, the contact line moves backward. To realize this effect, at each time step of computation, we should first obtain the local apparent contact angle at the contact points. Then, comparisons of θ with θ_R and θ_A are required. If $\theta \leqslant \theta_R$, θ in Eq. (14) should be replaced by θ_R; if $\theta \geqslant \theta_A$, θ in Eq. (14) should be replaced by θ_A; else, θ in Eq. (14) remains unchanged [6,12,41]. Here we can see that the hysteresis effect is prescribed by two parameters: advancing angle and receding angle, which depend on the properties of fluids and solids [40]. This simple implementation can realize contact angle hysteresis effect, no matter if the hysteresis is caused by roughness or chemical inhomogeneities.

III. RESULTS AND DISCUSSION

A. Droplet on a solid wall with prescribed wettability

First, droplet contacts with an ideal wall for six different angles are simulated. As shown in Fig. 2 ($\alpha = 0^\circ$, $g = 0$), the top and bottom boundaries are solid walls and simple bounce-back is applied. Periodic boundary conditions are applied to the left and right boundaries. Hereafter, the same boundary conditions are adopted in all cases unless otherwise specified. In these simulations, a semicircular droplet was initialized in a computational domain 201×101. The angle θ was specified in Eq. (14). After an evolution process, the droplet would reach an equilibrium state. Figure 3 shows the six different equilibrium contact angles achieved. The specified θ is also illustrated in the bottom of each subfigure. We find the final contact angle obtained is highly consistent with the specified one. The final contact angle is measured through a geometric formula [14]. In the geometric formula, if one knows the chord length "L" and the distance from the chord to the peak of the arc "h", then the contact angle θ can be calculated through $\tan(\theta) = hL/[(\frac{L}{2})^2 - h^2]$. In the six cases, the maximum discrepancy between the measured and the specified contact angles is less than 1°. It demonstrates the scheme is very accurate for the treatment of wettability on an ideal wall.

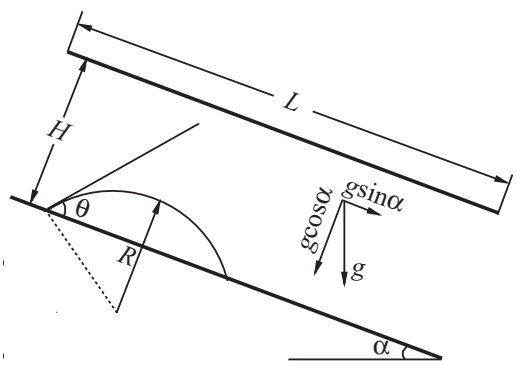

FIG. 2. Schematic of a droplet on an inclined wall.

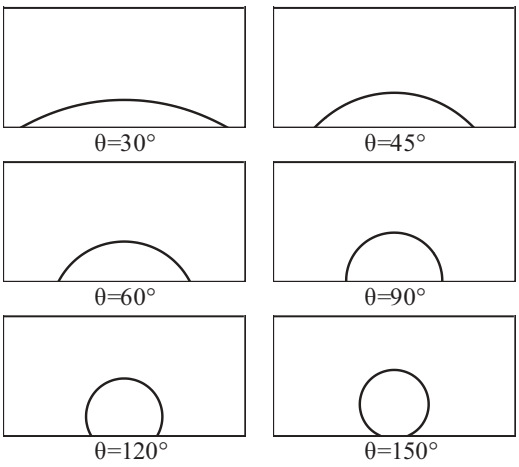

FIG. 3. Different contact angles are achieved by putting different specified θ into Eq. (14).

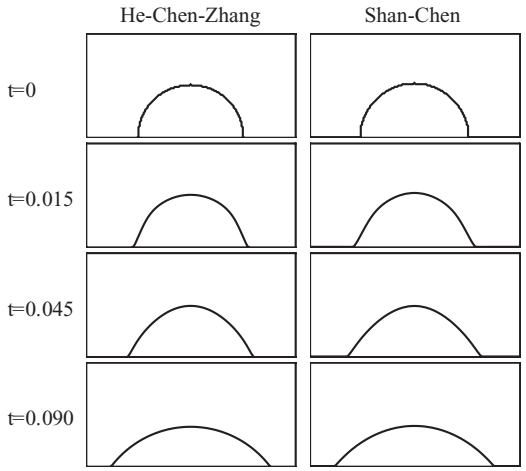

FIG. 4. Comparison of interface profiles of an initially semicircular droplet spreading towards the equilibrium state. The left and right columns are results of simulation using the He-Chen-Zhang model and the Shan-Chen model, respectively. In both simulations, $\rho_l/\rho_g = 10.46$, $\mu_l/\mu_g = 10.46$, and Oh $= 0.0553$.

An evolution process from the initial semicircular droplet to an equilibrium state is illustrated in the following in detail. The simulation result obtained by the He-Chen-Zhang model is compared with that obtained by the Shan-Chen model [22]. For comparison, a nondimensional parameter Oh is introduced,

$$\mathrm{Oh} = \frac{\mu_l}{\sqrt{\rho_l H \sigma}}, \tag{18}$$

where H is the width of channel and σ is surface tension. In the He-Chen-Zhang simulation, the surface tension is controlled by the parameter κ. Usually, σ is proportional to κ. The relationship between σ and κ is determined by numerical simulations of a droplet immersed in another fluid. Through measuring the pressure difference (Δp) between outside and inside the droplet at the equilibrium state, σ is determined by $\sigma = \Delta p R$, where R is the radius of the droplet. Through several tests and linear fit, we get $\sigma = 0.01098\kappa$.

The computational domain is 601×201 in both the Shan-Chen and the He-Chen-Zhang simulations. In the Shan-Chen model, the Carnahan-Starling equation of state is used with $T = 0.3102$, $a = 4$, $b = 4$. The corresponding densities of liquid and gas are $\rho_l = 0.296$ and $\rho_g = 0.0283$, respectively. The corresponding surface tension is $\sigma = 0.01344$, which is measured through Laplace law. The other settings are $\tau_l = \tau_g = 1$, $\rho_w = 0.18$. ρ_w represents the density of solid wall, and different contact angles can be obtained by adjusting its value [42]. Here, with $\rho_w = 0.18$, the corresponding equilibrium contact angle is 48° and we also set $\theta = 48°$ in the He-Chen-Zhang simulation. The left and right columns in Fig. 4 are the simulation results from the He-Chen-Zhang model and the Shan-Chen model, respectively. The time is normalized by $\sqrt{\rho_l R^3/\sigma}$. From Fig. 4, we can see that the interface profiles at time $t = 0.015, 0.045, 0.09$ obtained from the two simulations agree well with each other. Hence, we can see that the geometric formulation is also appropriate to simulate dynamic contact line problems. To further validate this point, another moving contact line problem is investigated and compared with result of the finite element method (FEM).

In the following part, the dynamical behavior of a droplet slipping on a neutrally wetting solid wall ($\theta = 90°$) under gravity is simulated (refer to Fig. 2 with $\alpha = 90°$). In this flow, two important nondimensional numbers are Bond number (Bo) and Reynolds number (Re), which are defined as,

$$\mathrm{Bo} = \frac{\rho_l g H^2}{\sigma}, \tag{19}$$

$$\mathrm{Re} = \frac{H\sqrt{gH}}{\nu_l}, \tag{20}$$

where g is the applied gravity, $\sqrt{gH}$ is chosen as the characteristic velocity. In the simulation, Bo $= 16.459$, Re $= 27.885$, $\mu_l/\mu_g = 10.46$. The computational domain is 601×201, $R/H = 0.25$. The evolutions of the droplet obtained from the LB model and FEM are compared in Fig. 5. Both the positions and shapes of the droplet obtained from the LBM agree very well with those of the FEM. Obviously, the scheme for wetting condition without hysteresis can achieve reliable result.

Furthermore, to validate our scheme for 3D cases, an initially hemispherical droplet under gravity spreading on a heterogeneous surface is simulated. The computational domain is $201 \times 201 \times 101$. The droplet is set at the center of the wall and has radius of 40 l.u. The wall is supposed to be hydrophilic, except for the intersecting hydrophobic strips. In the strip areas, the contact angle is set to be $\theta = 100°$, and in the other area, $\theta = 45°$. The nondimensional parameters are Bo $=$ 45.719, Re $= 30$. Our simulation is almost identical to that in Ref. [43], except the density ratio. Figure 6 shows the evolution of the droplet at different times. We can see that the height of the droplet decreases and the contact area increases on the whole due to the gravity. The droplet experiences a process of spreading symmetrically into four hydrophilic sections but in the hydrophobic strips, it contracts inward slightly. Hence, different wettabilities can be achieved by specifying different θs into Eq. (15). The evolution of the droplet is consistent with that in Ref. [43].

Through the above tests of the droplet behaviors on an ideal wall, it is confirmed that the LBM combined with the wetting boundary treatment is a good tool to study moving contact line problems without hysteresis [17,18,35].

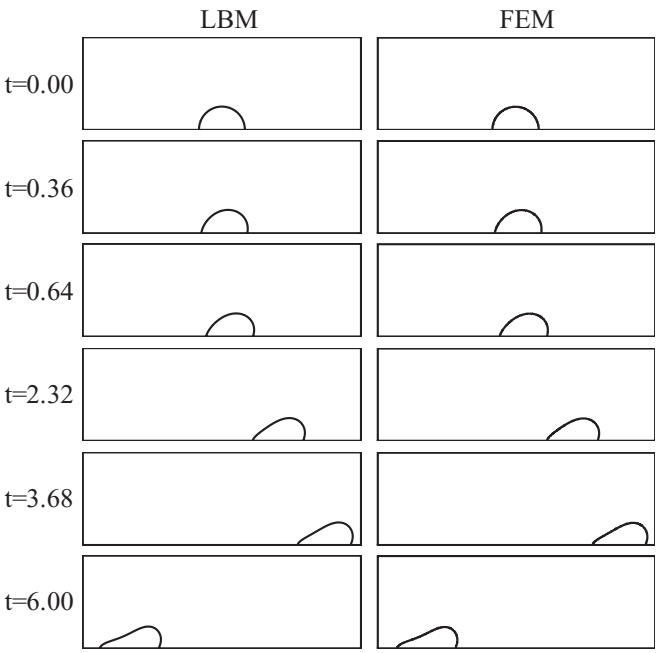

FIG. 5. Comparison of shape and position of a droplet slipping on a wall under gravity at different times. The time is normalized by $\sqrt{H/g}$. The left and the right are the results of the LBM and FEM, respectively.

B. Droplet on a nonideal wall with contact angle hysteresis

Droplet moving on a nonideal wall with contact hysteresis is an important research topic. In this section, the wetting boundary conditions are also tested for contact angle hysteresis.

1. Droplet slipping in shear flows

In this flow, an initially semicircle droplet deforms or slips in a shear flow driven by an upper plane moving with a constant velocity U.

Qualitative simulation results about effect of contact angle hysteresis are given in Fig. 7. There are four typical motion modes of the contact points due to four specified hysteresis windows. In Fig. 7(a), both the upstream and downstream contact angles are always inside the hysteresis window $(0°,180°)$, so the two corresponding contact points are pinned on the wall at all times. In Fig. 7(b), the upstream contact angle varies from the right angle to acute angles, so it is always in the range $(0°,110°)$; consequently, the upstream contact point cannot move. For the downstream contact point, at early stages it is pinned as the contact angle is less than 110°, and later it moves due to the contact angle greater than 110°. In Fig. 7(c), the downstream contact angle varies from the right angle to obtuse angles, which are always in the range $(70°,180°)$, so the downstream contact point remains immobile. For the upstream contact point, at early stages it is pinned due to the contact angle greater than 70°, and later it moves due to the contact angle less than 70°. Figure 7(d) shows that at early stages the droplet deforms and keeps pinned; subsequently, the two contact angles do not fall into the specified hysteresis window and the whole droplet slips.

Effect of contact angle hysteresis is also tested through 3D cases. In our simulations, initially, a 3D hemispherical droplet is resting on a solid plane in a Couette flow, where the upper wall moves rightward and the bottom wall remains stationary. In our 3D simulations, four typical motion modes for the contact lines as those in the 2D study (i.e., Fig. 7) are also achieved. Two of the four modes are shown in Figs. 8 and 9. In the figures, the shapes of contact lines at different times are also

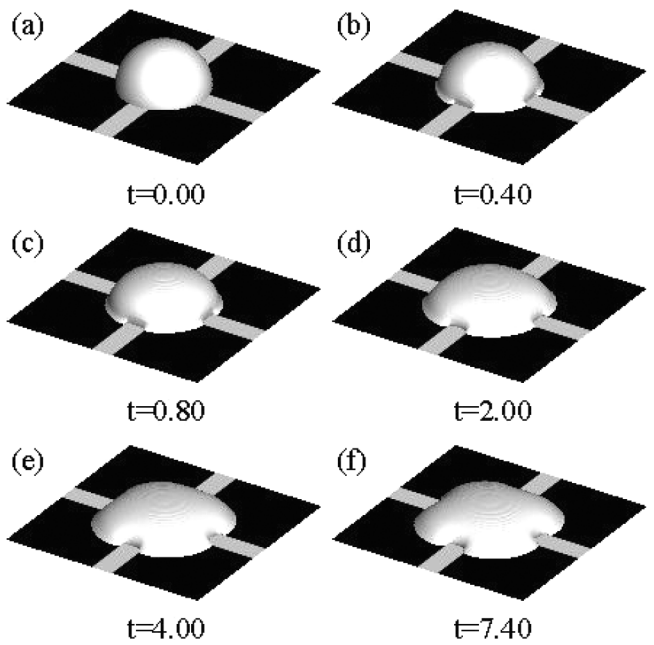

FIG. 6. A three-dimensional droplet spreading on a heterogeneous surface with intersecting strips that have opposite wettability. The time is normalized by $\sqrt{H/g}$.

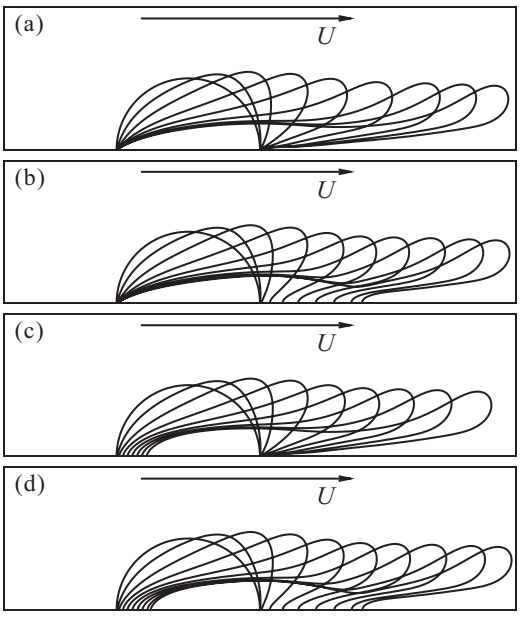

FIG. 7. Four typical motion modes of contact points by specifying contact angle hysteresis effect in the He-Chen-Zhang model. $(a)\,\theta_R = 0°, \theta_A = 180°$; $(b)\,\theta_R = 0°, \theta_A = 110°$; $(c)\,\theta_R = 70°, \theta_A = 180°$; $(d)\,\theta_R = 70°, \theta_A = 110°$.

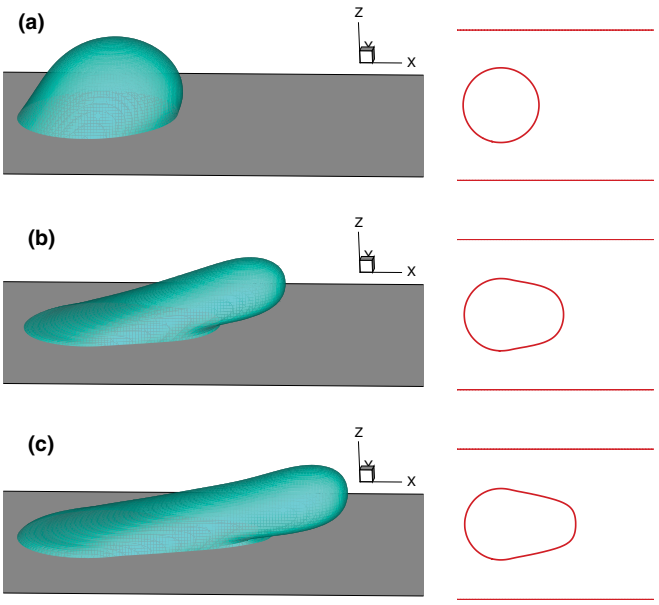

FIG. 8. (Color online) Movement of a 3D hemispherical droplet, which is driven by a shear flow at (a) t = 2000 t.s., (b) t = 6500 t.s., (c) t = 8000 t.s. The hysteresis window is $\theta_R = 0^\circ, \theta_A = 110^\circ$. The shapes of contact lines at different times are shown in the right column.

shown in the right column. Figure 8 is obtained through setting the hysteresis window (0°,110°). The motion mode is similar to that of Fig. 7(b), in which the upstream contact line keeps stationary while the downstream section moves. In this motion mode, the contact area increases. Figure 9 is obtained through setting the hysteresis window (70°,180°). The motion mode is similar to that of Fig. 7(c), in which the upstream section moves while the downstream section remains stationary. In

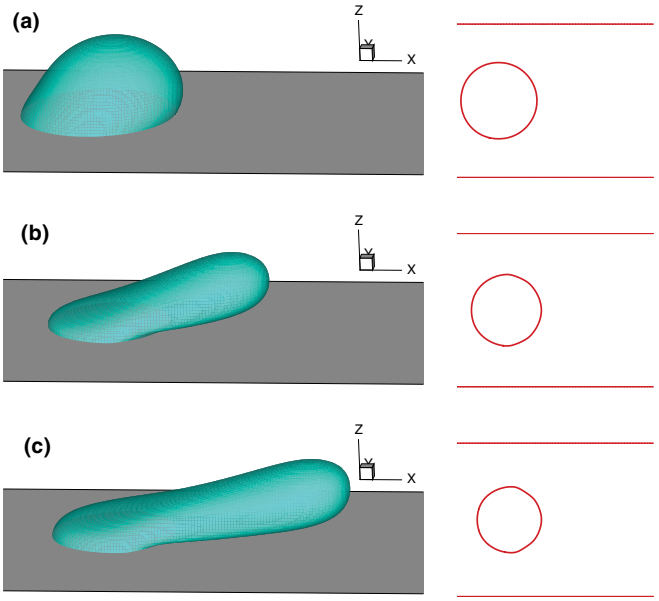

FIG. 9. (Color online) Movement of a 3D hemispherical droplet driven by a shear flow at (a) $t = 2000$ t.s., (b) $t = 6000$ t.s., (c) $t = 8000$ t.s. The hysteresis window is $\theta_R = 70^\circ, \theta_A = 180^\circ$. The shapes of contact lines at different times are shown in the right column.

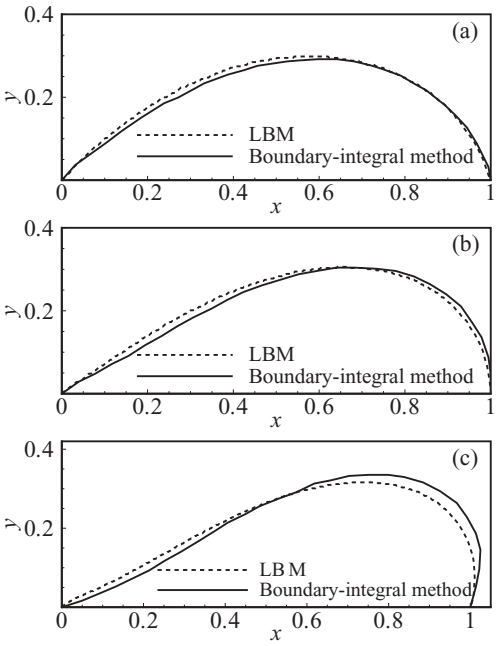

FIG. 10. Comparison of interface profiles when droplets reach stationary states under shear flows. The capillary number takes the value (a) Ca = 0.05, (b) Ca = 0.10, (c) Ca = 0.15, respectively.

this mode, the contact area decreases. Both the 2D and 3D results of simulations are consistent with the predictions about the typical phenomena of contact angle hysteresis.

In a shear flow of low capillary number, the droplet deforms or creeps along the solid wall. In this small section, we compared our LBM result about this flow with the result of Schleizer *et al.* [13], as Dupont *et al.* did [6]. Because the He-Chen-Zhang model is not able to simulate cases of two-phase flows with identical densities, here the Lee-Lin model [27] is adopted. In our study, $\rho_l/\rho_g = 1$ and $\mu_l/\mu_g = 1$. In Fig. 10, the LBM results of droplet deformations are compared with those obtained by the boundary-integral method [13]. In these simulations, we set $\theta_R = 10^\circ, \theta_A = 170^\circ$, according to the study of Dupont *et al.* [6], a wide contact angle hysteresis window, to make the two contact points immobile at low capillary number ($\mathrm{Ca} = \mu_l U/\sigma$). The solid and dashed lines represent the interface profiles of a steady droplet under three different Ca s. The good agreement shows that the LBM simulation is a suitable tool for modeling contact line problems with hysteresis in shear flows.

2. *Droplet slipping under gravity*

The behavior of a droplet on an inclined wall under gravity may be similar to that in a shear flow. However, several benchmark problems about a droplet slipping under gravity can further validate our scheme. Hence, the behaviors of a droplet on a nonideal wall under gravity are simulated. As expected, under certain circumstances significant different behaviors of a droplet on ideal surfaces and nonideal surfaces were observed. As an example, the results of Bo = 0.519 are shown in Fig. 11. At this Bo, a droplet cannot stay stationary and keep slipping on an ideal wall; however, it can be pinned on a nonideal wall

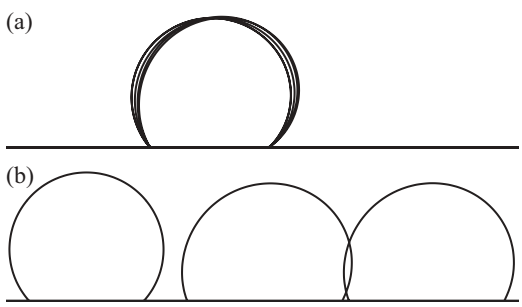

FIG. 11. Significantly different behaviors of a droplet on a nonideal wall and an ideal wall. Bo = 0.549, Re = 12.471, $\alpha = 55^\circ$. (a) $\theta_R = 115^\circ$, $\theta_A = 145^\circ$, the droplet deforms and keeps stationary; (b) the droplet slips all along on an ideal wall.

due to hysteresis. In the simulation, the upper and lower bounds of the hysteresis window is set as $\theta_R = 115^\circ$, $\theta_A = 145^\circ$.

For the hysteresis cases, when a droplet sticks to a wall, the tangential component (parallel to the wall) of the gravity and the surface tension applied to the droplet are in balance [44,45]. Hence, an equation about force balance along the wall direction is written as [6]

$$\rho_l A_l g \sin\alpha = \sigma(\cos\theta_u - \cos\theta_d), \tag{21}$$

where A_l is the area of liquid droplet in 2D simulations, and θ_u and θ_d denote the upstream contact angle and downstream contact angle, respectively. Equation (21) can also be written as

$$\sin\alpha = (\cos\theta_u - \cos\theta_d)/\mathrm{Eo}, \tag{22}$$

where Eo is the Eotvos number that is defined as $\mathrm{Eo} = \rho_l A_l g/\sigma$. Several cases of droplets pinning have been tested on nonideal walls with different obliquities. Figure 12 shows that $\sin\alpha$ has a good linear relationship with $(\cos\theta_u - \cos\theta_d)/\mathrm{Eo}$, and the slope of the fit line is about 1.05, which is very close to unity, the theoretical one.

Furthermore, we compared the present LBM [27] results of droplet deformations with those obtained by Dupont *et al.* [6]. The computational domain is 400 × 100. A semicircular droplet with a radius $R = 40$ is put on an inclined wall. Nine cases with different contact angle hysteresis windows, inclined angle α, and Eo as those investigated by Dupont *et al.* [6] are simulated. In these LB simulations, the Lee-Lin model is used and $\rho_l/\rho_g = 1000$, $\mu_l/\mu_g = 500$. The comparison between LBM results and those of Dupont *et al.* [6] is shown in Fig. 13.

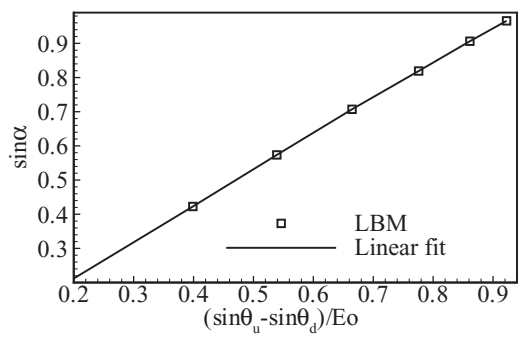

FIG. 12. Validation of Eq. (22) when a droplet is pinned on a wall. The slope of the linear fit is 1.05.

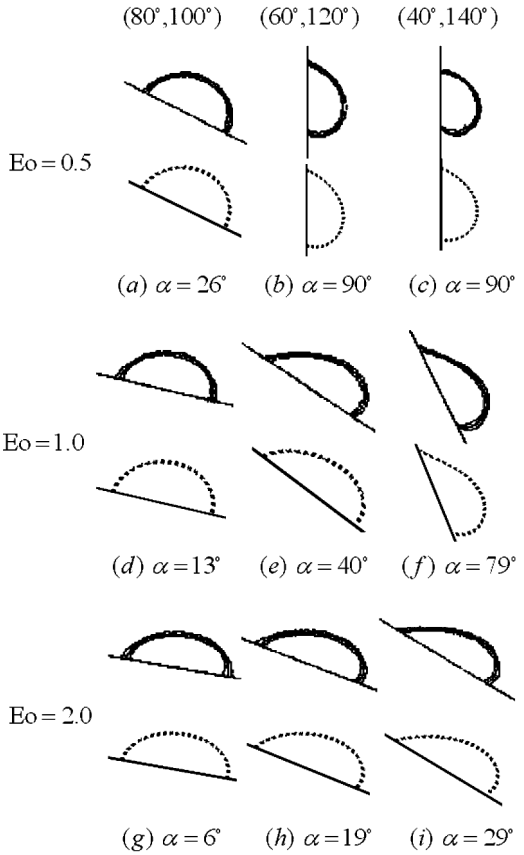

FIG. 13. Comparison of interface profiles when droplets reach steady states on an inclined wall. α denotes the tilt angle. The solid and dashed lines represent the shapes obtained by Dupont *et al.* [6] and our LBM scheme, respectively. The hysteresis window of the cases in left, middle, and right columns are $(\theta_R,\theta_A) = (80^\circ,100^\circ)$, $(60^\circ,120^\circ)$, $(40^\circ,140^\circ)$, respectively.

Here, $\mathrm{Eo} = \rho_l g R^2/\sigma$ and cases of Eo = 0.5, 1.0, 2.0 were simulated. From the figure we can see that when droplets reach steady states under gravity, the interface shapes obtained through LBM agree very well with those obtained by Dupont *et al.* [6]. This quantitative comparison further confirms that our scheme is reliable for contact line problems with hysteresis effect.

Currently, lots of interesting phenomena involving contact angle hysteresis effect have been found and studied experimentally [46,47]. For instance, Mettu *et al.* studied the role of contact angle hysteresis in the motion of liquid drops on surfaces induced by asymmetric vibration [46]. Luo *et al.* observed the stretching and contraction of the drops on an inclined wall mimic the motion of an inchworm by tuning contact angle hysteresis [47].

In the following part, we tried to recover the "creep of an inchworm" using our LBM to demonstrate that our scheme is able to handle more complex contact line dynamics. The "inchworm" here is referred to as the droplet we simulated. In our simulation, computational domain is 400 × 100. The initial droplet radius is 50 l.u. and the initial apparent contact angle is 60°. The other parameters are $\rho_l/\rho_g = 10.46$, $\mu_l/\mu_g = 10.46$. To make the droplet creep, two different hysteresis windows $(\theta_R,\theta_A)_1 = (55^\circ,85^\circ)$ (the first window), $(\theta_R,\theta_A)_2 = (30^\circ,60^\circ)$

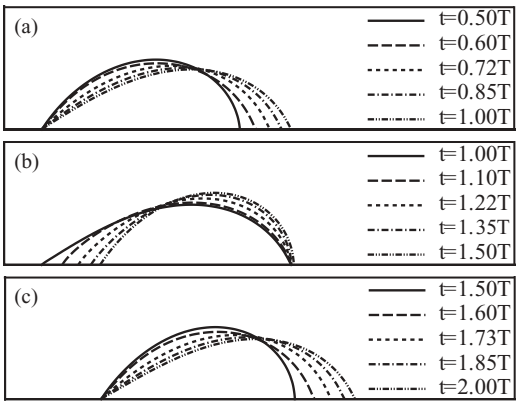

FIG. 14. Stretching and contraction of a droplet crawling like an inchworm due to change of hysteresis window periodically. The tilt angle of the inclined wall is $\alpha = 60^\circ$. Bo = 2.286, Re = 21.213.

(the second window) have been implemented alternately after a period of $T/2 = 1.414$ (the characteristic time is chosen as $\sqrt{H/g}$).

The "creep of the droplet" is shown in Fig. 14. In Fig. 14, at the beginning, the upstream contact angle reduces with time (could be seen in Fig. 15, $0.5T \sim 1.0T$), it always belongs to the second hysteresis window. Consequently, the upstream contact point is pinned on the wall; meanwhile, the downstream contact angle is slightly larger than 60° and outside the hysteresis window, so the corresponding downstream contact point slips, which could be seen in Fig. 14(a). When the hysteresis window shifts to the first one ($1.0T \sim 1.5T$), the downstream contact angle increases from about 60°; therefore, it is inside the window and the downstream contact point stops slipping; on the contrary, the upstream contact angle becomes less than 55°, so the upstream contact point does not remain pinned and starts to move, which could be seen in Fig. 14(b). The positions of the upstream and downstream contact points as functions of time are shown in Fig. 16. The distance between the two points is the wetting length L, which elongates and shortens periodically as shown in Fig. 16. Figure 14(c) shows a new cycle of "creeping" motions. Qualitatively, the creeping motion of the droplet is recovered.

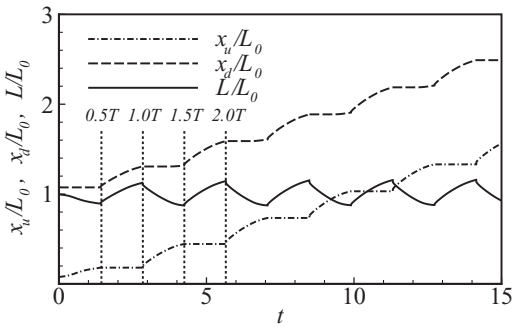

FIG. 15. Both the upstream contact angle (symbol of triangle) and the downstream contact angle (symbol of square) as functions of time.

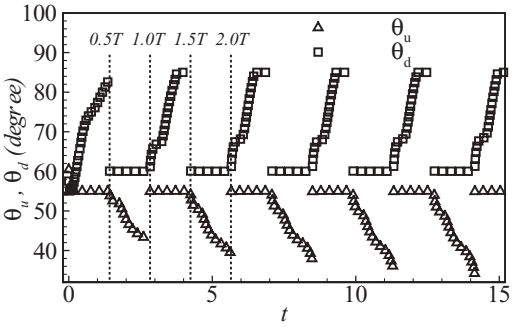

FIG. 16. Nondimensional wetting length and positions of the two contact points vary with time. L_0 is the initial wetting length. x_u,x_d are the positions of upstream contact point and downstream contact point, respectively.

IV. CONCLUSION

In this paper, the geometric formulation [36] is incorporated into the He-Chen-Zhang model and the Lee-Lin model, which are applied to study droplet slipping on ideal surfaces and nonideal surfaces.

For ideal surfaces, we obtained desired contact angle accurately. The spreading processes of an initially semicircle droplet toward an equilibrium contact angle and a droplet slipping on neutral wetting solids under gravity are simulated. The corresponding results agree well with the results of the Shan-Chen model and finite element method, respectively.

For nonideal surfaces, contact angle hysteresis is described by θ_R and θ_A. When a droplet is subjected to a shear flow, four typical motion modes are observed. Furthermore, the shapes of a droplet under three different Ca s, are in good accord with those obtained from the boundary-integral method. When a droplet is under gravity, droplet behaviors are totally different with and without contact angle hysteresis. When a droplet is pinned on solids due to hysteresis, the force balance between the surface tension and gravity parallel to the wall is validated. Besides, nine different cases about a droplet in equilibrium states on inclined walls under gravity are studied, and the interface shapes match very well with those studied by Dupont *et al.* [6]. The present methods could also qualitatively recover the complex and interesting motion of a droplet like a creeping inchworm, which was observed in the experiment [47].

Hence, the present scheme is a promising tool in studying the dynamical behaviors of droplets on either ideal walls (without hysteresis) or nonideal walls (with hysteresis), in which the hysteresis property has been known from the experiments.

Instead of reproducing a known result, LBM may be used as a predictive tool. It is worthy to note that, recently, Colosqui *et al.* [28] presented a LBM model to simulate wetting dynamics mesoscopically. Although presently it is unknown how to specify the macroscopic variables, such as hysteresis window (advancing and receding angles) in the model, it may be promising to predict the contact angle hysteresis. In our future study, we would try to connect the mesoscopic descriptions [28] with the macroscopic phenomena.

ACKNOWLEDGMENTS

L. Wang thanks H. Ding for his instructive suggestions and beneficial discussions and P. Gao for providing FEM simulation results. Thanks are due also to K. Mu, who helped us in computing some cases. This work is supported by the National Natural Science Foundation of China (NSFC) (Grant No. 10802085).

[1] C. Huh and L. E. Scriven, J. Colloid Interface Sci. **35**, 85 (1971).
[2] L. M. Hocking, J. Fluid Mech. **76**, 801 (1976).
[3] B. Elizabeth, V. Dussan, and S. H. Davis, J. Fluid Mech. **65**, 71 (1974).
[4] T. D. Blake and J. M. Haynes, J. Colloid Interface Sci. **30**, 421 (1969).
[5] V. V. Khatavkar, P. D. Anderson, and H. E. H. Meijer, J. Fluid Mech. **572**, 367 (2007).
[6] J.-B. Dupont and D. Legendre, J. Comput. Phys. **229**, 2453 (2010).
[7] P. Dimitrakopoulos and J. J. L. Higdon, J. Fluid Mech. **336**, 351 (1997).
[8] P. Dimitrakopoulos and J. J. L. Higdon, J. Fluid Mech. **377**, 189 (1998).
[9] P. Dimitrakopoulos and J. J. L. Higdon, J. Fluid Mech. **395**, 181 (1999).
[10] P. Dimitrakopoulos and J. J. L. Higdon, J. Fluid Mech. **435**, 327 (2001).
[11] H. Ding, M. N. H. Gilani, and P. D. M. Spelt, J. Fluid Mech. **644**, 217 (2010).
[12] P. D. M. Spelt, J. Comput. Phys. **207**, 389 (2005).
[13] A. D. Schleizer and R. T. Bonnecaze, J. Fluid Mech. **383**, 29 (1999).
[14] Q. Kang, D. Zhang, and S. Chen, Phys. Fluids **14**, 3203 (2002).
[15] D. Iwahara, H. Shinto, M. Miyahara, and K. Higashitani, Langmuir **19**, 9086 (2003).
[16] J. Zhang and D. Y. Kwok, Langmuir **20**, 8137 (2004).
[17] M. Latva-Kokko and D. H. Rothman, Phys. Rev. Lett. **98**, 254503 (2007).
[18] M. Sbragaglia, K. Sugiyama, and L. Biferale, J. Fluid Mech. **614**, 471 (2008).
[19] Y. H. Kim, W. Choi, and J. S. Lee, Microfluid. Nanofluid. **10**, 173 (2011).
[20] D. H. Rothman and J. M. Keller, J. Stat. Phys. **52**, 1119 (1988).
[21] A. K. Gunstensen, D. H. Rothman, S. Zaleski, and G. Zanetti, Phys. Rev. A **43**, 4320 (1991).
[22] X. Shan and H. Chen, Phys. Rev. E **47**, 1815 (1993).
[23] X. Shan and H. Chen, Phys. Rev. E **49**, 2941 (1994).
[24] M. R. Swift, W. R. Osborn, and J. M. Yeomans, Phys. Rev. Lett. **75**, 830 (1995).
[25] X. He, S. Chen, and R. Zhang, J. Comput. Phys. **152**, 642 (1999).
[26] T. Inamuro, T. Ogata, S. Tajima, and N. Konishi, J. Comput. Phys. **198**, 628 (2004).
[27] T. Lee and L. Liu, J. Comput. Phys. **229**, 8045 (2010).
[28] C. E. Colosqui, M. E. Kavousanakis, A. G. Papathanasiou, and I. G. Kevrekidis, arXiv:1202.6130 (2012).
[29] H. Kusumaatmaja and J. M. Yeomans, Langmuir **23**, 956 (2008).
[30] F. Varnik *et al.*, Phys. Fluids **20**, 072104 (2008).
[31] C. Pirat, M. Sbragaglia, A. M. Peters, B. M. Borkent, R. G. H. Lammertink, M. Wessling, and D. Lohse, Europhys. Lett. **81**, 66002 (2008).
[32] H. Kusumaatmaja and J. M. Yeomans, Soft Matter **5**, 2704 (2009).
[33] L. Fan, H. Fang, and Z. Lin, Phys. Rev. E **63**, 051603 (2001).
[34] D. Jacqmin, J. Fluid Mech. **402**, 57 (2000).
[35] A. J. Briant, A. J. Wagner, and J. M. Yeomans, Phys. Rev. E **69**, 031602 (2004).
[36] H. Ding and P. D. M. Spelt, Phys. Rev. E **75**, 046708 (2007).
[37] D. d'Humiéres, I. Ginzburg, M. Krafczyk, P. Lallemand, and L.-S. Luo, Trans. R. Soc. Lond. A **360**, 437 (2002).
[38] R. Zhang, X. He, and S. Chen, Comput. Phys. Commun. **129**, 121 (2000).
[39] T. Lee and L. Liu, Phys. Rev. E **78**, 017702 (2008).
[40] P. G. de Gennes, Rev. Mod. Phys. **57**, 827 (1985).
[41] H. Ding and P. D. M. Spelt, J. Fluid Mech. **599**, 341 (2008).
[42] R. Benzi, L. Biferale, M. Sbragaglia, S. Succi, and F. Toschi, Phys. Rev. E **74**, 021509 (2006).
[43] Y. Yan and Y. Zu, J. Comput. Phys. **227**, 763 (2007).
[44] C. G. L. Furmidge, J. Colloid Sci. **17**, 309 (1962).
[45] V. C. G. Dussan and R. T. P. Chow, J. Fluid Mech. **137**, 1 (1983).
[46] S. Mettu and M. K. Chaudhury, Langmuir **27**, 10327 (2011).
[47] M. Luo, R. Gupta, and J. Frechette, Appl. Mat. Interfaces **4**, 890 (2012).